Nanoscale

PAPER

View Article Online
View Journal | View Issue

Cite this: *Nanoscale*, 2026, **18**, 375

On-chip EPR spectrometry of metalloproteins using superconducting lumped element resonators

Carlos Marcuello, †[a,b,f] David Rodriguez, †[c] María Carmen Pallarés, [a,b] Daniel Granados, [d] Olivier Roubeau, [a] Fernando Luis, [a] Alicia Gomez *[c] and Anabel Lostao *[a,b,e]

We report electron paramagnetic resonance experiments performed on myoglobin hemeproteins using a chip hosting 6 superconducting lumped element resonators with resonance frequencies between 1.94 and 2.11 GHz. Successive layers of myoglobin were deposited onto the inductors of four of them using dip-pen nanolithography, a technique based on atomic force microscopy. A combination of atomic force and confocal microscopies estimated the number of protein molecules in each deposit, which ranges from 8.6×10^{11} (one dip-pen layer) to 3.33×10^{12} (four dip-pen layers). Two reference bulk samples were pipetted from the same solution onto the remaining two resonators. The microwave transmission of the device, measured at 11 mK, shows evidence of the coupling of protein spins to the photon excitations of all resonators. In particular, the resonance broadening measured as a function of magnetic field provides the spin resonance absorption spectrum. The analysis suggests that proteins tend to self-orient on the chip. It also allows estimating the single spin to single photon coupling strength, which is around 9 Hz. This high coupling value suggests that dip-pen nanolithography gives rise to a close to optimum interface between the molecules and the chip surface. The developed methodology combines an increase in sensitivity of at least three orders of magnitude with the ability to characterize multiple samples in a single experiment, opening the door to a highly sensitive multi-analyte detection technology.

Received 23rd July 2025,
Accepted 25th November 2025

DOI: 10.1039/d5nr03119b

rsc.li/nanoscale

Introduction

Sensitive label-free sensor platforms are in high demand in our society, for example, for the early detection of fingerprint analytes, viral or bacterial protein antigens, or nucleic acids associated with certain pathologies. In this work, we focus on the study of metalloproteins, a large and diverse group of proteins that contain metal ions, such as manganese, iron, copper, cobalt, zinc, or nickel, which are directly bound to the protein structure. These proteins are essential for living organisms, participating in a wide range of biological processes.[1]

Understanding the relation between structure and function is essential for developing therapeutic strategies and diagnostic tools. Among these proteins, ubiquitous hemeproteins are of particular interest; they contain an iron-porphyrin group called heme, which plays a central role in determining their function and physicochemical properties.[2]

Here, we consider myoglobin as a reference system with a ferric heme iron Fe^{3+} (d^5) in a high-spin configuration, $S = 5/2$. The Fe(III) heme centre of myoglobin is involved in transporting oxygen from the bloodstream to the muscles,[3] the oxidation of lipids,[4] and the scavenging and detoxifying of harmful compounds like nitric oxide or reactive oxygen species.[5] Myoglobin testing has also seen a recent growing interest due to the release of myoglobin from the muscles into the blood during a heart attack, being one of the earliest markers of myocardial infarction, or severe muscle damage associated with different pathologies.[6] These processes can result in dangerous levels of myoglobin in the organism that can be detected in blood and urine. Too much myoglobin can overwhelm the kidneys and lead to kidney failure.[7]

Different myoglobin proteins can be found in cardiac tissues and other mammalian muscles. They are formed by a single polypeptide chain folded in eight α-helices that attach

[a]*Instituto de Nanociencia y Materiales de Aragón (INMA), CSIC-Universidad de Zaragoza, Plaza San Francisco s/n, 50009 Zaragoza, Spain.*
E-mail: aglostao@unizar.es
[b]*Laboratorio de Microscopias Avanzadas (LMA), Universidad de Zaragoza, Ed. I+D+i. Mariano Esquillor s/n, 50018 Zaragoza, Spain*
[c]*Centro de Astrobiología, INTA-CSIC, Ctra. Torrejón-Ajalvir km.4, Torrejón de Ardoz, 28850 Madrid, Spain. E-mail: agomez@cab.inta-csic.es*
[d]*IMDEA Nanociencia, Cantoblanco, 28049 Madrid, Spain*
[e]*Fundación ARAID, Av. Ranillas 1-D, 50018 Zaragoza, Spain*
[f]*Biofisika Institute (CSICUPV/EHU) and Department of Biochemistry and Molecular Biology, University of the Basque Country, Leioa 48940, Spain*
†These authors contributed equally to this work.

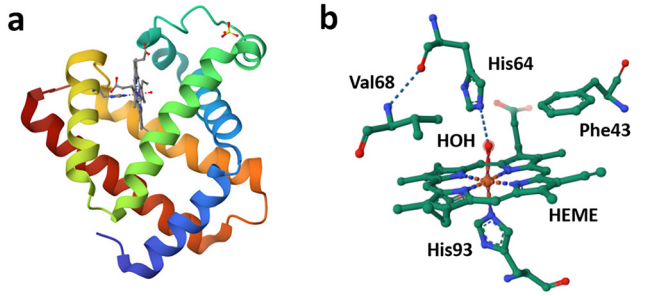

Fig. 1 (a) Three-dimensional molecular structure of the myoglobin protein from equine heart that binds the heme group (PDB code 1WLA).[8] (b) Structure of the active site of met-myoglobin (Fe^{3+}) bound to the hydroxide of a water molecule. In the active site of oxy-myoglobin, the O_2 molecule binds to the iron atom, forming a Fe–O–O bent structure, and iron adopts an octahedral coordination geometry, where the distal histidine (His64) forms an N–H···O hydrogen bond with O_2.

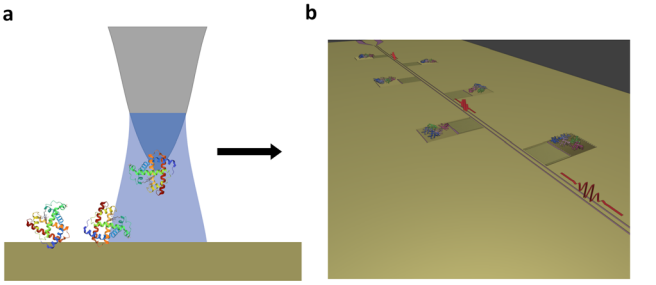

Fig. 2 (a) Schematic representation of the myoglobin ink transfer process onto the device surface by dip-pen nanolithography developed in this work. (b) Three-dimensional rendering of a superconducting device hosting six superconducting lumped element resonators with myoglobin molecules (not at scale) deposited on their inductors.

an heme group, capable of binding molecular oxygen with two histidine amino acids of the protein structure (Fig. 1). Myoglobin can be found in four redox states through its heme group, (i) deoxy-myoglobin, that presents Fe^{2+} bound to water at the interior of muscles; oxy-myoglobin, that presents Fe^{2+} bound to molecular oxygen (*e.g.* surface of meat in air); carboxy-myoglobin, with Fe^{2+} bound to carbon monoxide; and met-myoglobin, carrying Fe^{3+} bound to hydroxide (Fig. 1b).

Electron paramagnetic resonance (EPR) spectroscopy is a non-invasive technique used to analyze unpaired electron spins present in a variety of materials, such as paramagnetic dopants in inorganic semiconductors and ceramics, or molecule-based materials like organic free radicals and molecular magnets. EPR has also been widely employed to investigate the oxidation state and the local coordination of the metal center in different metalloproteins,[9–11] including myoglobin.[12–15] As such, commercial EPR systems offer a powerful tool for characterizing these biological materials. However, their sensitivity typically requires the use of samples containing more than 10^{15}–10^{16} spins,[15–17] which can limit the study of single crystals or the detection of trace amounts of metalloproteins present in certain biological samples.

Micro-EPR devices provide a way to improve sensitivity by reducing the electromagnetic mode volume of the EPR cavities.[18] The ultimate detection limits have been achieved using cavities defined on superconducting circuits, fabricated onto chips employing top-down lithography techniques. These circuits form the basis for circuit quantum electrodynamics,[19] a widespread technology for reading out and interconnecting different qubit realizations[20–23] and quantum memories.[24] Used as spin resonance devices, they can show mode volumes in the femto-L range,[25,26] and reach few spins or even the single spin sensitivity when combined with quantum-limited readout electronics.[27,28] However, in this limit, the integration of the spins within the electromagnetic field mode volume defined by the circuit becomes critical. For this reason, most of these experiments have been performed on model spin systems, often located inside the chip substrate. In addition, the most sensitive detection schemes severely limit the range of frequencies that can be investigated. Therefore, combining very high sensitivity with the ability to explore a wide variety of materials remains a challenge. Here, we address this challenge *via* a new circuit design (Fig. 2b) and by exploiting nanolithography techniques to achieve a close to optimal chip-to-sample interface.

The circuit, illustrated in Fig. 2b, consists of six superconducting Lumped Element Resonators (LERs), essentially a resonant inductor–capacitor circuit, parallel coupled to a common readout transmission line. This geometry enables flexible design of the key cavity parameters, such as the resonance frequency f_r, field mode volume, and the quality factor Q, without affecting the overall chip transmission. Moreover, following the strategy used in kinetic inductance detectors for astronomical observations,[29] all resonators can be simultaneously probed, allowing parallel characterization. Myoglobin samples were accurately integrated into the circuits by means of dip-pen nanolithography (DPN) based on atomic force microscopy (AFM),[30] shown in Fig. 2a. This technique allows the precise deposition on a surface of almost any type of inorganic or organic molecules,[31] biomolecules,[32,33] or nanomaterials with nanometric resolution and at ambient conditions.[34] DPN enabled the transfer of multiple layers onto particular regions of each LER or onto adequate substrates for complementary characterization studies of the shape, size, and topography of the protein deposits. Here, we report on the properties of the chip, the integration and the *in situ* characterization of the protein deposits, and the results of microwave transmission experiments, which provide direct information on their spin resonance spectrum.

Results and discussion

Chip description and characterization

The chip consists of six resonators capacitively coupled to a common readout transmission line. Each resonator follows the Lumped Element Resonator (LER) design (Fig. 3a), in which the capacitor C and inductor L are defined geometrically.[35] From now on, the resonators are labelled LER 1 to LER 6, ordered by increasing resonance frequency. The inductor geo-

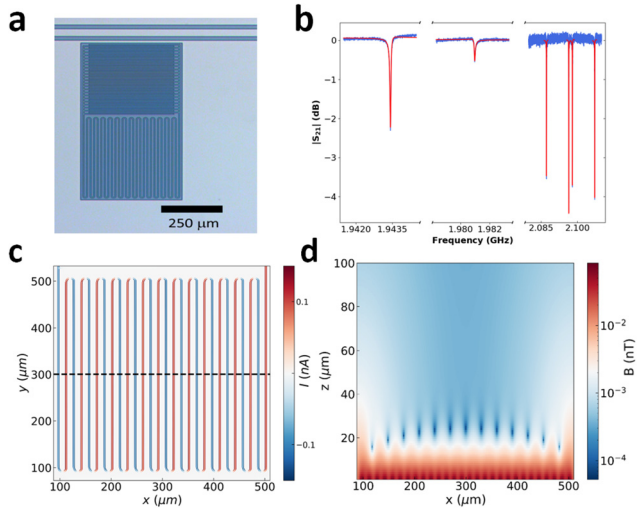

Fig. 3 (a) Optical microscopy image of one of the fabricated Nb LERs, showing the *LC* resonator capacitively coupled to the readout line (top part of the image). (b) Microwave transmission measured at T = 11 mK as a function of the readout frequency (blue lines). Each transmission minimum corresponds to the resonance of a LER coupled to the readout line. The red line is a least-squares fit of each LER transmission based on eqn (1). (c) On-resonance current distribution in the resonator inductor. Here, the plane x–y defines the chip's surface, whereas z measures the distance from it. (d) Magnetic field distribution generated by the inductor in the x–z plane, calculated for y = 300 μm, marked by a dashed horizontal line in (c).

metry determines the magnetic field distribution and, therefore, the sensitive part.[36] In our design, a meandered inductor layout is employed to enhance the magnetic field strength near the chip surface and the area is chosen to match the characteristic size of the protein deposits. Fig. 3c and d illustrate the current distribution on resonance and the generated magnetic field. The resonance frequency, $f_r = 1/\sqrt{LC}$, is tuned *via* the capacitor design, while keeping the inductor dimensions and therefore the magnetic field volume, fixed.

The microwave transmission of the "bare" chip was characterized prior to myoglobin deposition.[37,38] The LERs resonances appear as transmission dips at their resonance frequencies, which range between 1.9 GHz and 2.2 GHz (see Fig. 3b), in excellent agreement with the simulated ones. The data are fitted using the following equation:

$$S_{21} = \left| 1 - \frac{\kappa_c e^{i\phi}}{i(f_r - f) + \kappa} \right| \quad (1)$$

where ϕ is a phase that accounts for the asymmetries in the resonance shape caused by Fano interferences. The fit allows extracting f_r as well as the external (arising from the coupling to the readout line) κ_c and the total κ photon damping rates. The latter, which also includes internal damping within the resonator, is close to 30 kHz both before and after myoglobin deposition, indicating that the deposition process does not significantly affect resonator losses. These losses lead to mean LER quality factors $Q \approx 7 \times 10^4$.

Preparation and deposition of myoglobin samples

In this work, we used buffered solutions of myoglobin from equine heart at different concentrations, using glycerol as an additive, prepared as described in the Experimental section. Protein patterning was done with a high-performance commercial DPN system. The ink composition, AFM probes selection, parameter deposition, and environmental conditions were optimized using SiO_2 marked substrates (see ref. 39 and Fig. S1 from the SI). These test assays were also useful to calibrate the approximate number of protein molecules deposited on each layer for each experimental condition (Fig. S1). Final depositions onto the chip were carried out by immersing the AFM tip in an ink solution drop. A number of layers were then transferred through sequential deposition steps at each of the different LERs, until the whole inductor was covered by the ink (from 1 to 4 deposition layers on LERs 6, 4, 5 and 3, respectively), as shown in Fig. 4. LERs 1 and 2 were also covered with 100 nL of 50 and 5 mM inks (Fig. S2 and S3). This allows a comparison of the spin signals of bulk and patterned samples in the same experiment.

In situ characterization of the protein deposits: estimation of the spin number in the deposits

The volumes of the samples deposited onto each LER were determined by confocal microscopy measurements, as shown in Fig. 4. For this, the morphology of the deposits (Fig. S2 and S3) was first compared to the bare LER surface before the first

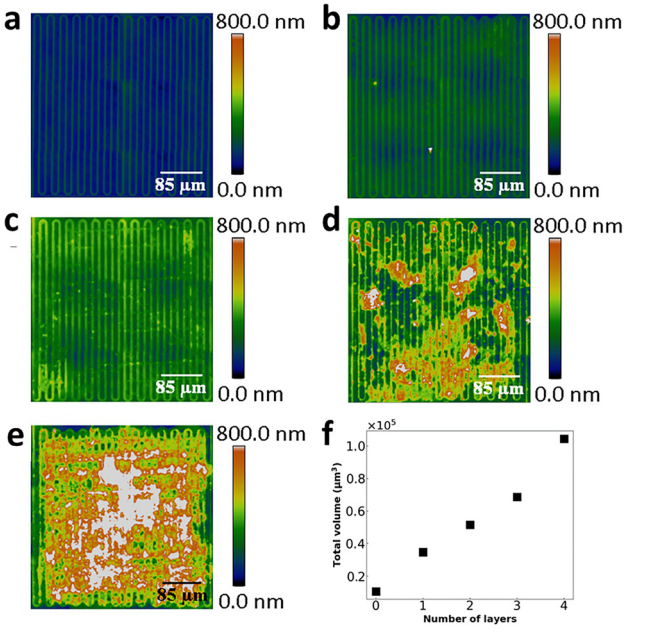

Fig. 4 Confocal images of LER 3 in different stages of the protein deposition process: (a) bare LER before myoglobin deposition, (b–e) the same LER after the sequential deposition of 1, 2, 3, and 4 myoglobin layers by DPN, respectively. The scan size is 425 μm × 425 μm. The colour scales are fixed to the maximum height observed for all the images (800 nm) to better discern the increase in sample thickness after the transfer of successive layers by DPN. (f) Total volume estimated for the different number of deposited layers.

deposition step (Fig. 4a and S2a, S3a). This method gave reliable results for the topography of myoglobin deposits fabricated by DPN (LERs 3 to 6), but failed in the case of myoglobin microdroplets (LERs 1 and 2) due to the formation of ripples caused by the Moiré-pattern effect.[40] These interferences are induced by the close overlapping in frequencies of the exposed surface by a light source. As shown by Fig. S3g, the successive transfer of myoglobin layers leads to an increase in deposit thickness, as well as to a larger protein coverage of the LER inductor. The estimated volumes of the DPN deposits range from approximately 2.4×10^4 μm^3 to 9.4×10^4 μm^3 for 1 to 4 deposition steps. These volumes were then converted into the number of molecules N using their concentration in the inks. Both are listed in Table 1.

The results show a close to linear increase in protein volume with the number of deposition steps (Fig. 4f), thus supporting that subsequent depositions do not erase the underlying sample and, therefore, demonstrating that DPN allows controlling the number of protein molecules transferred to specific areas of the device.

The deposits were also analysed by X-ray photoelectron spectroscopy (see section S3 in the SI). The spectra are very similar to that of the lyophilized protein, showing the presence of the expected elements, in addition to Si and Nb from the substrate (Table S1 and Fig. S4). Furthermore, high-resolution spectra of bulk powder and the 4-layer DPN deposit were analysed in detail. Again, they show signals that confirm the successful transfer of the hemeprotein to the chip, plus some others related to the chip itself and remains from the ink solvent (Fig. S5).

On-chip broadband magnetic spectroscopy

To perform a preliminary characterization of the protein microwave absorption spectrum, a myoglobin sample was deposited on top of the readout transmission line. The measured results are shown in Fig. 5a.

To compensate for the line attenuation and the presence of unavoidable spurious modes (horizontal lines in Fig. 5a), the transmission is normalized by subtracting data measured at different magnetic fields, as described previously.[41] This allows for the clear identification of microwave absorption features, which depend on magnetic field B, and can therefore be associated with resonant spin transitions in myoglobin. The Fe^{3+} center of each molecule has an $S = 5/2$ spin with a large magnetic anisotropy, which can be parameterized by a second-order uniaxial parameter $D = 9.26$ cm^{-1}.[14] In the frequency range of these experiments, only transitions between the spin states $m = \pm 1/2$ from the lowest lying Kramer's doublet, which are also the only ones populated at 11 mK, can be studied. The myoglobin spin can then be approximated by an effective $S = 1/2$ system[12,14] with $g_{\mathrm{eff},\perp} = 5.92$, $g_{\mathrm{eff},z} = g_{\mathrm{eff},\parallel} = 2$. The two absorption lines visible in the broadband spectrum agree with the extremal absorption edges associated with these principal values of the g-tensor. In a randomly oriented sample, the maximum change in absorption with B occurs approximately at these edge fields. Therefore, as it also happens with conventional EPR data measured in the derivative mode, they are enhanced by the normalization of the transmission data.

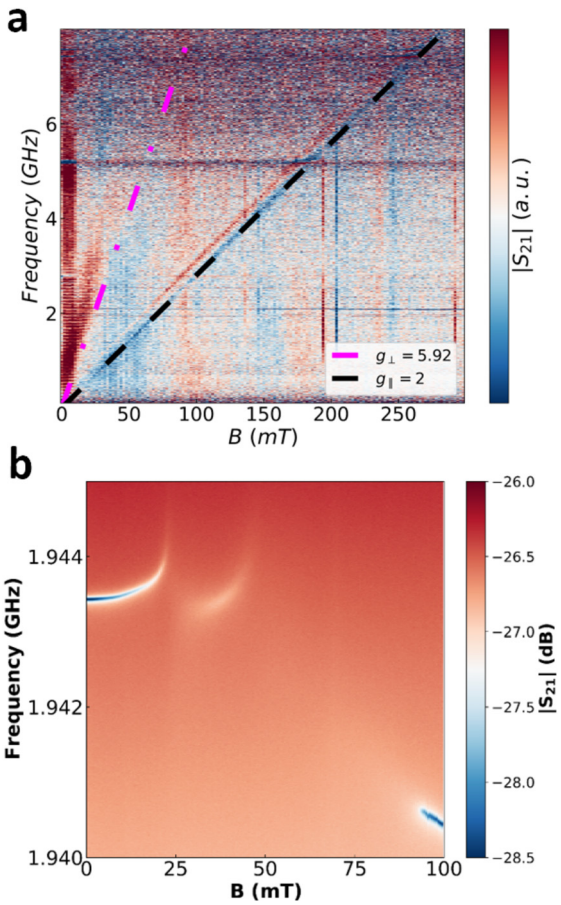

Fig. 5 (a) Normalized microwave transmission measured at $T = 11$ mK as a function of external magnetic field B on a transmission line coupled to myoglobin. The two main features are indicated with dashed lines. Magenta corresponds to a slope of $g_{\mathrm{eff},\perp} = 5.92$ while black represents $g_{\mathrm{eff},\parallel} = 2$. The normalization is done by subtracting data measured at two magnetic fields separated by 10 mT, and dividing the result by data measured at $B = 0$. (b) Microwave transmission measured at $T = 11$ mK near the resonance frequency of LER 1 and as a function of B. A 0.1 μL droplet of a 50 mM myoglobin solution was deposited onto the inductor of this LER.

Table 1 Summary of the volumes and corresponding number of spins estimated for the deposits patterned with DPN on LERs 3 to 6

LER	DPN layers	Volume (μm^3)	N (10^{12} spins)
3	4	93 829	3.33
4	2	40 859	1.45
5	3	57 903	2.05
6	1	24 256	0.86

On-chip electron paramagnetic resonance

EPR experiments were performed by measuring the microwave transmission at frequencies close to the resonances of the six

LERs as a function of magnetic field. The power used in the measurements was $P = -60$ dBm, corresponding to $n \sim 10^9$ photons in the resonator. We first discuss results obtained for LERs 1 and 2, covered with myoglobin microdroplets, which provide a characterization of the bulk EPR spectrum under the same conditions. Results obtained for LER 1 at $T = 11$ mK are shown in Fig. 5b. The parabolic field dependence of the resonant frequency is attributed to the effect that B has on the properties of the superconducting film, as it is also observed in bare chips, not coupled to any magnetic sample (see example in Fig. S6). In addition, fingerprints of the coupling between the cavity photons and spin transitions are observed, much more clearly than in the broadband spectrum. The coupling shifts the resonance frequency, leading to characteristic anticrossings, and drastically reduces the resonance visibility, *i.e.*, the transmission dip associated with the bare LER (Fig. 5b). Two broad absorption signals are observed, the first between $B = 20$–30 mT and the second between 50 and 90 mT. The lowest and highest magnetic fields approximately agree with the resonant fields expected for the principal values of the g tensor, thus with resonant conditions with molecules having their magnetic z-axis either perpendicular or parallel to the external magnetic field. The absorption intensities reveal a convolution of the number of molecules in a given orientation and of the transition matrix elements for this condition. The results are therefore compatible with the known magnetic properties of this protein,[12] and with a distribution in the orientations of myoglobin molecules within the droplets.

In order to probe the sensitivity of the EPR characterization using these LERs, the amount of myoglobin in different LERs was varied as described in previous sections. Fig. 6 shows data obtained for LERs 3, 5, 4, and 6, where the number of DPN layers was 4, 3, 2, and 1, respectively (see Table 1). As can be seen, in all of them the transmission shows the same absorption features that were observed for the bulk-like droplets, albeit with weaker intensities. The spread in magnetic field comes from the distribution in molecular orientations and from the strength G of the collective spin–photon coupling. As the number of molecules decreases, the visibility of the two absorption signals also decreases. Still, they remain visible even for the sample consisting of a single DPN layer (LER 6). These results show that the combination of superconducting LERs and a suitable deposition method provides the ability to study, in a single chip, the EPR spectra of a given biological material for different frequency windows and, in this case, for different sample sizes.

A quantitative analysis of these data allows obtaining additional information on the interaction of the myoglobin deposits with the cavity photons. For this, we fit the LER response at each magnetic field. The transmission data measured for LERs 3–6 do not show any evidence for the splitting of the photon modes that characterizes the coherent, or strong spin–photon coupling regime. Then, it is possible to describe these data using a formalism valid for the weak coupling regime, when G is much smaller than the spin resonance linewidth γ. The microwave transmission is described by a modified version of eqn (1), which now includes the effect of the magnetic sample

$$S_{21} = \left| 1 - \frac{\kappa_c e^{i\phi}}{i(f_r - f) + \tilde{\kappa}} \right| \quad (2)$$

where $\tilde{\kappa} \geq \kappa$ is an effective photon decay rate. The broadening of the photon modes reflects their interaction with the spins, which becomes maximum every time a spin transition frequency f_s becomes close to f_r. Then, a plot of $\tilde{\kappa}$ as a function of B provides direct information on the EPR absorption spectrum. Data measured for LER 6 (1 DPN layer) are shown in Fig. 7. They show the two broad absorption bands already visible in the 2D transmission plots of Fig. 6, which correspond, respectively, to molecules with the z-axis being either close to parallel or close to orthogonal to the magnetic field orientation. In the weak coupling limit, it is possible to derive expressions to fit these results. The coupling to molecules with a given orientation (parameterized by the angle θ) gives a photon broadening expressed as

$$\tilde{\kappa} = \kappa + \frac{G(\theta)^2 \gamma}{(f_s(\theta) - f_r)^2 + \gamma^2} \quad (3)$$

where the spin resonance frequency $f_s(\theta) = \sqrt{(g_z{}^2 \cos^2(\theta) + g_\perp{}^2 \sin^2(\theta)}$ and the collective coupling strength of these molecules $G(\theta) \simeq N^{1/2} G_1 \sqrt{n(\theta)}$. Here, $n(\theta)$ is

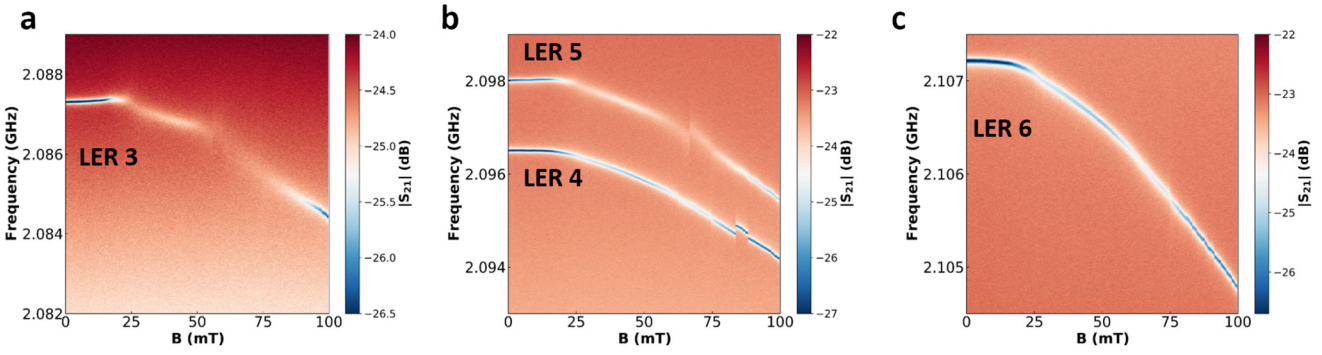

Fig. 6 Microwave transmission measured at $T = 11$ mK as a function of frequency and applied magnetic field for LER 3 (a), LERs 4 and 5 (b), and LER 6 (c).

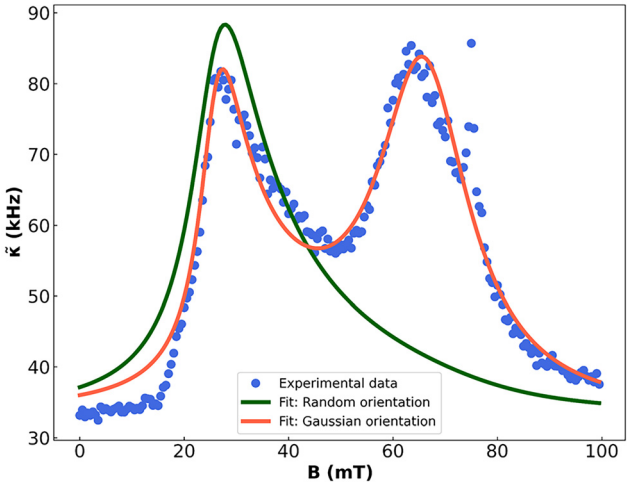

Fig. 7 Resonance linewidth $\tilde{\kappa}$ of LER6, hosting a single DPN layer of myoglobin on its inductor, measured at T = 11 mK as a function of magnetic field (blue dots). The green and red solid lines are least-squares fits based on eqn (3), corresponding to gaussian distributions for random and oriented protein molecular orientation, respectively. For the latter, the best fit parameters are the collective spin–photon coupling $G \simeq N^{1/2} G_1$ = 6.23 MHz, the spin resonance linewidth γ = 335 MHz, and the center θ_0 = 11.6° and width $\delta\theta_0$ = 0.1° of the distribution of molecular orientations $n(\theta)$, given by eqn (4).

the normalized distribution of molecular orientations within each deposit, and G_1 is the single spin–photon coupling, averaged over the spatial and angular distribution of the microwave field generated by the inductor (see Fig. 3c and d). The overall $\tilde{\kappa}$ can then be obtained by averaging eqn (3) over θ.

In order to extract the different parameters, first κ of the bare resonator was extracted by fitting its resonance measured at B = 0, where it is assumed that the resonator's properties remain unaffected by its coupling to myoglobin spins. This leaves G_1, the spin linewidth γ, and the angular distribution $n(\theta)$ as free parameters. The fitting procedure is explained in detail in section S4. The results are compared to the experimental data in Fig. 7 for LER 6 and in Fig. S7, S8 and S9 for LERs 3, 4 and 5, respectively.

The simulation obtained for a random molecular orientation, when $n(\theta) = \sin\theta \mathrm{d}\theta$, fails to correctly account for the intensity ratio of both resonance lines. This suggests that myoglobin molecules have a certain tendency to self-align. This effect has been taken into account by setting

$$n(\theta) = \left(\eta e^{\frac{-(\theta-\theta_0)^2}{2\delta\theta_0^2}} + (1-\eta) \right) \sin\theta \mathrm{d}\theta \qquad (4)$$

where the preferred angle θ_0, the angular distribution width $\delta\theta_0$ and η are adjustable parameters. A reasonably good fit was obtained for θ_0 = 11.6° and η = 0.997. A more detailed explanation of how these parameters have been estimated can be found in section S4 in the SI, which includes a Table S2 with values obtained for all DPN deposits. The results of these fits suggest that the spin–photon coupling is dominated by a majority of myoglobin molecules aligned with their z-axis close to the magnetic field orientation. The fit also gives the average collective coupling $G \simeq N^{1/2} G_1$. The results obtained for the 4 myoglobin DPN deposits are given in Table 2. Besides, eqn (2) and (3) allow calculating the full microwave transmission. An illustrative example for LER 6 is shown in Fig. 8 (for LERs 3, 4, and 5 see Fig. S7, S8, and S9).

Table 2 Average collective spin–photon coupling G and spin resonance linewidth γ obtained for the four myoglobin samples deposited by DPN onto LERs 3 to 6

LER	DPN layers	G (MHz)	γ (MHz)
3	4	18.14 ± 0.16	334 ± 11
5	3	16.75 ± 0.23	334 ± 15
4	2	6.44 ± 0.04	334 ± 9
6	1	6.23 ± 0.04	335 ± 8

Finally, using the number of spins N determined for each myoglobin deposit (Table 1), the mean coupling per spin $G_1 = G/\sqrt{N}$ can be estimated using the G values from Table 2. We find $\tilde{G}_1 \approx 9$ Hz. This value must be regarded as a lower bound. Even very close to the chip surface, where the protein DPN deposits are located, the microwave magnetic field generated by the resonator inductor remains inhomogeneous, being approximately 5 times higher on top of the meander inductor lines (Fig. 3d) than in the regions separating them. This means that the actual number of molecules that contribute most to the collective G is significantly smaller than N. Still, G_1 is higher than the values previously obtained for VO-porphyrin molecules deposited by Langmuir–Blodgett techniques on both CPW resonators[42] and on LERs.[39]

Experimental

Micro fabrication techniques

The chip was fabricated in a cleanroom with a controlled environment. The resonators are designed using CAD-based software, and their RF response is simulated using the commercial software Sonnet.[43] From these simulations, the resonance frequency f_r and the coupling to the transmission line can be estimated. The nanofabrication process begins with the deposition of a 100 nm thick niobium (Nb) layer on a 350 μm thick silicon substrate by means of DC magnetron sputtering from AJA International, Inc. with a base pressure better than 10^{-8} Torr. An argon pressure of 1.5 mTorr and a power of 100 W lead to a growth rate of 0.77 Å s^{-1}. Then, the design is transferred to the superconducting film using a maskless laser lithography system (Heidelberg Instruments). An AZnLOF negative resist is spinned at 5000 rpm for one minute, followed by a 100 °C heat. After exposure, the sample is post-baked at 110 °C for 60 seconds and developed using AZ developer for 60 seconds at ambient temperature. Finally, the Nb layer is etched using a reactive ion etcher with a mixture of Ar and SF_6 (Oxford Instruments). The final chip is cleaned in an acetone

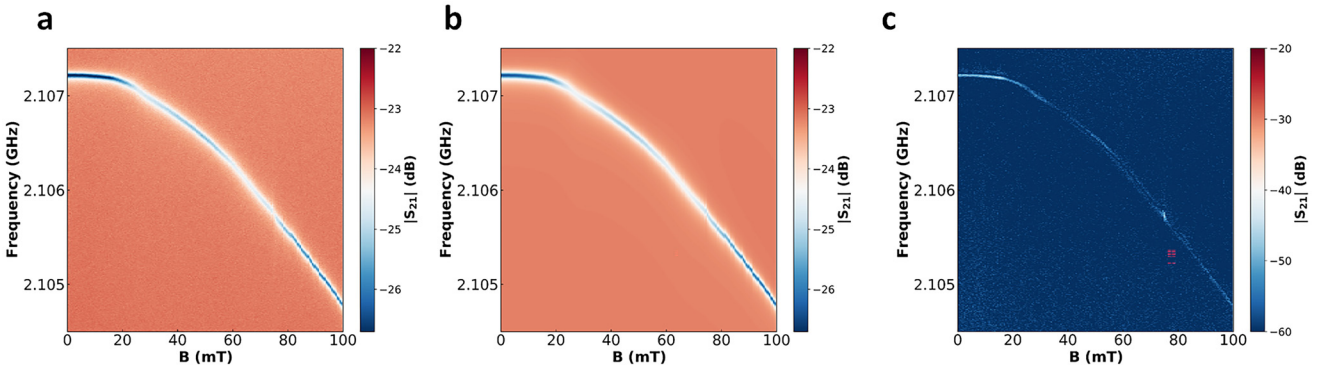

Fig. 8 (a) 2D colour plot of the microwave transmission measured at T = 11 mK near the resonance frequency of LER 6. (b) Microwave transmission calculated with eqn (3) and the parameters obtained in Fig. 7. (c) Residuals of the model and the experimental data.

and isopropanol bath to remove the unexposed resist. Fig. 3a shows an image of one of the fabricated LERs.

Myoglobin sample preparation

Ink solutions of 5 and 50 mM myoglobin from equine heart (≥90.0%, Sigma-Aldrich) were prepared in a 50 mM MOPS (3-(*N*-morpholino)propanesulfonic acid, ≥99.5%, Sigma-Aldrich) buffer at pH 7.0, in the presence of 20% glycerol (v : v, ≥99.5%, Sigma-Aldrich) and stored in darkness at 4 °C. Glycerol increases the viscosity and therefore retards evaporation of liquid samples, which helps the deposition of protein solutions[44] (Fig. 2a). Moreover, glycerol is a well-known agent that prevents protein degradation at cryogenic temperatures, enabling the subsequent EPR measurements at low temperatures with functional samples.[15]

Dip-pen nanolithography

Protein patterning was developed with a high-performance DPN5000 setup based on AFM (NanoInk, Inc.). The ink composition, AFM probes selection, parameter deposition, and environmental conditions were optimized using SiO_2 marked substrates.[39] Final depositions were carried out using silicon nitride rectangular ORC8 AFM probes exhibiting a stiffness constant of 0.1 N m^{-1}, provided with pyramidal tips (Bruker Probes) at 25 °C and 35% relative humidity. The chip was cleaned with IPA and imaged with confocal microscopy before each deposition process. The tip was immersed several times in a 0.1 μL ink solution drop located on the resonator surface, and then located with the help of an optical microscope. A successive number of layers was then transferred through sequential deposition steps at the different LERs. The deposition was run by successive line-writing until the whole chip was covered by the ink. The topographies of the bare LERs were previously calibrated (Fig. S2 and Fig. 4a). After each deposition step, the chip was placed inside a desiccator under vacuum for 72 hours. One, two, three, and four deposits with 5 mM myoglobin ink solutions were carried out on LERs 6, 4, 5, and 3, respectively (Fig. 4). Additionally, 0.1 μL droplets of 5 mM and 50 mM myoglobin inks were pipetted on LERs numbers 2 and 1, respectively (Fig. S2 and S3).

Confocal microscopy

A confocal microscope PL 2300 (Sensofar) was used to acquire 3D topography maps of the myoglobin dry deposits formed on the LERs. The measurements were performed with a ×20 microscope objective and with a numerical aperture of 0.50. The working distance was optimized to accurately converge the optical image of the tested areas. Arrays of 2 × 3 scan-field images were integrated to generate 500 μm × 500 μm topography maps. Raw data were processed using the Gwyddion software.[45] All the images were treated following the same procedure to prevent estimation errors associated with data handling. In order to estimate the volume of the dry deposits located on each LER, mask thresholds were defined as previously described.[46] First, the bare circuit topography was analyzed, and then the resulting volume was subtracted from the topography of each deposit.

The number of spins or myoglobin molecules located on each LER is obtained from the volume of the deposits calculated as described above and the volume of each protein molecule. The estimation of the unitary volume corresponding to a single molecule was calculated from the dimensions of the equine heart myoglobin atomic structure (Fig. 1a; PDB code: 1WLA[8]). This is approx. 27.9 nm^3 assuming that the protein structure exhibits a perfect parallelepiped-shaped block (3.5 nm × 2.1 nm × 3.8 nm). The contribution of glycerol molecules to the deposit volumes was neglected based on their low concentration in the ink and on their much smaller molecular size as compared to that of myoglobin.

Microwave transmission experiments

The microwave transmission was characterized using a vector network analyzer.[37,38] The chip was thermalized to the mixing chamber of a cryo-free Bluefors LD250 dilution refrigerator equipped with microwave coaxial lines, attenuators (input signals), and cryogenic amplifiers (output signals). A cryo-free superconducting magnet allows applying dc magnetic fields up to 1 T along the Z laboratory axis, parallel to the chip surface and the readout transmission line. The experiments were done under vacuum and at a base temperature of 11 mK.

Conclusions

The obtained results in this work show that a combination of top-down and bottom-up techniques enables performing multiple EPR experiments within a chip with sensitivities largely exceeding those of conventional EPR spectrometers. Here, dip-pen nanolithography, based on AFM, was used for a precise deposition of 1 to 4 myoglobin layers, controlling both the sample size and its location at the sensors. Besides, the ability to multiplex the readout of different superconducting resonators in a single chip has allowed measuring the magnetic resonance of all these samples within a single experiment, *i.e.*, under identical conditions, and to compare the results with those obtained *in situ* for bulk samples. The results show the potential of this device to characterize metalloprotein samples at the level of a few pL and in a temperature region inaccessible to commercial EPR systems. They are also compatible with the spin and magnetic anisotropy of myoglobin. Yet, data measured on the protein deposits show intensity ratios between the resonances associated with the two extreme molecular orientations that are at odd with that expected for randomly oriented spins in equilibrium. This might suggest that myoglobin molecules, or their heme groups, may exhibit certain preferential orientation. The information at hand does not allow providing a clear picture about the origin of this effect and more work would be required to explain it. We however consider it unlikely that DPN gives rise to any significant protein alignment, and the effect seems also present for droplets deposited by a micropipette. A surface interaction can also be discarded, as the same qualitative results are also observed for multilayers. An alternative, plausible explanation for this effect, as described in previous works,[47] could be the saturation of the EPR intensity caused in samples with very long spin relaxation times, T_1, such as myoglobin at very low temperatures.

Remarkably, the mean coupling value per spin ranges between 5–12 Hz, which largely exceeds values measured for vanadyl porphyrin MOFs samples transferred by Langmuir–Blodgett on LERs.[39] This confirms that patterning the molecules by DPN achieves a close to optimal interface with the chip, which is a critical requisite to achieve the maximum sensitivity. The same methodology can be applied to diverse materials relevant to biology or medicine. This includes the characterization of other metalloproteins with unpaired electrons, such as ferritin or hemoglobin, reactive oxygen species which play a major role in disorders like ischaemic inflammation diseases or cancer and undesirable or harmful free radicals or metal ions in food.[47] Besides, its sensitivity can be enhanced by locally reducing the width of the inductor line.[26]

Conflicts of interest

There are no conflicts to declare.

Data availability

Data shown in the main text figures are deposited at the FATMOLS community in the Zenodo repository at https://doi.org/10.5281/zenodo.17791193.

Supplementary information (SI) is available. Figures S1, S2 and S3 provide additional information regarding the protein deposits. Figures S4, S5 and Table S1 give information about X-ray photoelectron spectroscopy data. Figures S6, S7, S8, S9 and Table S2 provide further experimental and microwave transmission simulations data. See https://doi.org/10.1039/d5nr03119b.

Acknowledgements

The authors would like to thank Dr Inés García-Rubio of INMA for the productive discussion on myoglobin EPR signals. This research work has been funded by the European Commission – NextGenerationEU (Regulation EU 2020/2094), through CSIC's Quantum Technologies Platform (QTEP). This work has received support from grants TED2021-131447B-C21, TED2021-131447B-C22, and PID2022-137779OB-C41 funded by the Spanish MCIN/AEI/10.13039/501100011033, by the EU "NextGenerationEU"/PRTR, projects PID2020-118329RB-I00, PID2022-140923NB-C21, and by the "ERDF A way of making Europe". IMDEA Nanoscience and INMA acknowledge grants from the "Severo Ochoa" Programme for Centres of Excellence in R&D (CEX2020-001039-S and CEX2023001286-S) funded by MICIU/AEI/10.13039/501100011033. The authors also thank the Aragón Government (PLATON E31_23R and QMAD E09_23R).

References

1 S. Lippard and J. Berg, *Principles of Bioinorganic Chemistry*, University Science Books, 1994.
2 S. Chapman, S. Daff and A. Munro, in *Heme: the most versatile redox centre in biology?*, ed. H. Hill, P. Sadler and A. Thompson, Springer, 1997, pp. 39–70.
3 D. J. Garry and P. P. A. Mammen, *Hypoxia and the Circulation*, Boston, MA, 2007, pp. 181–193.
4 C. Baron and H. Andersen, *J. Agric. Food Chem.*, 2002, **50**, 3887–3897.
5 T. Quinting, A. K. Heymann, A. Bicker, T. Nauth, A. Bernardini, T. Hankeln, J. Fandrey and T. Schreiber, *Front. Endocrinol.*, 2021, **12**.
6 S. Aydin, K. Ugur, S. Aydin, İ. Sahin and M. Yardim, *Vasc. Health Risk Manage*, 2019, **15**, 1–10.
7 B. M. I. Cabral, S. N. Edding, J. P. Portocarrero and E. V. Lerma, *Disease-a-Month*, 2020, **66**, 101015.
8 R. Maurus, C. M. Overall, R. Bogumil, Y. Luo, A. G. Mauk, M. Smith and G. D. Brayer, *Biochim. Biophys. Acta*, 1997, **1341**, 1–13.
9 S. Van Doorslaer and E. Vinck, *Phys. Chem. Chem. Phys.*, 2007, **9**, 4620–4638.

10 S. Lyubenova, T. Maly, K. Zwicker, U. Brandt, B. Ludwig and T. Prisner, *Acc. Chem. Res.*, 2010, **43**, 181–189.
11 S. Van Doorslaer, *J. Magn. Reson.*, 2017, **280**, 79–88.
12 P. J. M. van Kan, E. van der Horst, E. J. Reijerse, P. J. M. van Bentum and W. R. Hagen, *J. Chem. Soc., Faraday Trans.*, 1998, **94**, 2975–2978.
13 I. García-Rubio, M. Fittipaldi, F. Trandafir and S. Van Doorslaer, *Inorg. Chem.*, 2008, **47**, 11294–11304.
14 M. Fittipaldi, I. García-Rubio, F. Trandafir, I. Gromov, A. Schweiger, A. Bouwen and S. Van Doorslaer, *J. Phys. Chem. B*, 2008, **112**, 3859–3870.
15 I. Serra, I. García-Rubio and S. Van Doorslaer, *Appl. Magn. Reson.*, 2022, **53**, 1105–1119.
16 L. Song, Z. Liu, P. Kaur, J. M. Esquiaqui, R. I. Hunter, S. Hill, G. M. Smith and G. E. Fanucci, *J. Magn. Reson.*, 2016, **265**, 188–196.
17 S. Roy, A. Nandi, P. Das and C. Mitra, *IOP SciNotes*, 2020, **1**, 035202.
18 N. Abhyankar, A. Agrawal, J. Campbell, T. Maly, P. Shrestha and V. Szalai, *Rev. Sci. Instrum.*, 2022, **93**, 101101.
19 A. Blais, A. L. Grimsmo, S. M. Girvin and A. Wallraff, *Rev. Mod. Phys.*, 2021, **93**, 025005.
20 A. Wallraff, D. I. Schuster, A. Blais, L. Frunzio, R. S. Huang, J. Majer, S. Kumar, S. M. Girvin and R. J. Schoelkopf, *Nature*, 2004, **431**, 162–167.
21 J. Majer, J. M. Chow, J. M. Gambetta, J. Koch, B. R. Johnson, J. A. Schreier, L. Frunzio, D. I. Schuster, A. A. Houck, A. Wallraff, A. Blais, M. H. Devoret, S. M. Girvin and R. J. Schoelkopf, *Nature*, 2007, **449**, 443–447.
22 X. Mi, J. V. Cady, D. M. Zajac, P. W. Deelman and J. R. Petta, *Science*, 2017, **355**, 156–158.
23 A. A. Clerk, K. W. Lehnert, P. Bertet, J. R. Petta and Y. Nakamura, *Nat. Phys.*, 2020, **16**, 257–267.
24 C. Grezes, Y. Kubo, B. Julsgaard, T. Umeda, J. Isoya, H. Sumiya, H. Abe, S. Onoda, T. Ohshima, K. Nakamura, I. Diniz, A. Auffeves, V. Jacques, J.-F. Roch, D. Vion, D. Esteve, K. Moelmer and P. Bertet, *C. R. Phys.*, 2016, **17**, 693–704.
25 V. Ranjan, S. Probst, B. Albanese, T. Schenkel, D. Vion, D. Esteve, J. J. L. Morton and P. Bertet, *Appl. Phys. Lett.*, 2020, **116**, 184002.
26 I. Gimeno, W. Kersten, M. C. Pallarés, P. Hermosilla, M. J. Martínez-Pérez, M. D. Jenkins, A. Angerer, C. Sánchez-Azqueta, D. Zueco, J. Majer, A. Lostao and F. Luis, *ACS Nano*, 2020, **14**, 8707–8715.
27 A. Bienfait, J. J. Pla, Y. Kubo, M. Stern, X. Zhou, C. C. Lo, C. D. Weis, T. Schenkel, M. L. W. Thewalt, D. Vion, D. Esteve, B. Julsgaard, K. Mølmer, J. J. L. Morton and P. Bertet, *Nat. Nanotechnol.*, 2016, **11**, 253–257.
28 Z. Wang, L. Balembois, M. Rančić, E. Billaud, M. Le Dantec, A. Ferrier, P. Goldner, S. Bertaina, T. Chanelière, D. Esteve, D. Vion, P. Bertet and E. Flurin, *Nature*, 2023, **619**, 276–281.
29 J. J. A. Baselmans, J. Bueno, S. J. C. Yates, O. Yurduseven, N. Llombart, K. Karatsu, A. M. Baryshev, L. Ferrari, A. Endo, D. J. Thoen, P. J. de Visser, R. M. J. Janssen, V. Murugesan, E. F. C. Driessen, G. Coiffard, J. Martin-Pintado, P. Hargrave and M. Griffin, *Astron. Astrophys.*, 2017, **601**, A89.
30 G. Liu, S. H. Petrosko, Z. Zheng and C. A. Mirkin, *Chem. Rev.*, 2020, **120**, 6009–6047.
31 M. J. Martínez-Pérez, E. Bellido, R. d. Miguel, J. Sesé, A. Lostao, C. Gómez-Moreno, D. Drung, T. Schurig, D. Ruiz-Molina and F. Luis, *Appl. Phys. Lett.*, 2011, **99**, 032504.
32 S. Sekula, J. Fuchs, S. Weg-Remers, P. Nagel, S. Schuppler, J. Fragala, N. Theilacker, M. Franzreb, C. Wingren, P. Ellmark, C. A. K. Borrebaeck, C. A. Mirkin, H. Fuchs and S. Lenhert, *Small*, 2008, **4**, 1785–1793.
33 E. Bellido, R. de Miguel, D. Ruiz-Molina, A. Lostao and D. Maspoch, *Adv. Mater.*, 2010, **22**, 352–355.
34 J.-H. Lee, C. K. Najeeb, G.-H. Nam, Y. Shin, J.-H. Lim and J.-H. Kim, *Chem. Mater.*, 2016, **28**, 6471–6476.
35 S. Doyle, P. Mauskopf, J. Naylon, A. Porch and C. Duncombe, *J. Low Temp. Phys.*, 2008, **151**, 530–536.
36 S. Weichselbaumer, P. Natzkin, C. W. Zollitsch, M. Weiler, R. Gross and H. Huebl, *Phys. Rev. Appl.*, 2019, **12**, 024021.
37 B. Aja, M. C. de Ory, L. d. l. Fuente, E. Artal, J. P. Pascual, M. T. Magaz, D. Granados and A. Gomez, *IEEE Trans. Microwave Theory Tech.*, 2021, **69**, 578–589.
38 M. Rubín-Osanz, M. C. de Ory, I. Gimeno, D. Granados, D. Zueco, A. Gomez and F. Luis, *Low Temp. Phys.*, 2024, **50**, 472–480.
39 I. Gimeno, F. Luis, C. Marcuello, M. C. Pallarés, A. Lostao, M. C. de Ory, A. Gomez, D. Granados, I. Tejedor, E. Natividad, A. Urtizberea and O. Roubeau, *J. Phys. Chem. C*, 2025, **129**, 973–982.
40 R. E. Brooks and L. O. Heflinger, *Appl. Opt.*, 1969, **8**, 935–939.
41 I. Gimeno, V. Rollano, D. Zueco, Y. Duan, M. C. de Ory, A. Gomez, A. Gaita-Ariño, C. Sánchez-Azqueta, T. Astner, D. Granados, S. Hill, J. Majer, E. Coronado and F. Luis, *Phys. Rev. Appl.*, 2023, **20**, 044070.
42 A. Urtizberea, E. Natividad, P. J. Alonso, L. Pérez-Martínez, M. A. Andrés, I. Gascón, I. Gimeno, F. Luis and O. Roubeau, *Mater. Horiz.*, 2020, **7**, 885–897.
43 https://www.sonnetsoftware.com/support.
44 E. Bellido, R. de Miguel, J. Sesé, D. Ruiz-Molina, A. Lostao and D. Maspoch, *Scanning*, 2010, **32**, 35–41.
45 D. Nečas and P. Klapetek, *Open Phys.*, 2012, **10**, 181–188.
46 C. Marcuello, G. A. Frempong, M. Balsera, M. Medina and A. Lostao, *Antioxidants*, 2021, **10**, 1437.
47 A. Smirnov, *Electron Spin Resonance in Food Science*, Academic Press, 2017, pp. 83–109.